A computational view of the brain plasticity at rest

Invernizzi, Azzurra

DOI:
10.33612/diss.183130118

Chapter 3

Assessing uncertainty and reliability of connective field estimations from resting state fMRI activity at 3T

Based on:
*Invernizzi A **
*Gravel N**
Haak KV,
Renken RJ
Cornelissen FW (2021)

*These authors contributed equally to this work

Front. Neurosci. 15:625309. doi: 10.3389/fnins.2021.625309

ABSTRACT

Connective Field (CF) modeling estimates the local spatial integration between signals in distinct cortical visual field areas. As we have shown previously using 7T data, CF can reveal the visuotopic organization of visual cortical areas even when applied to BOLD activity recorded in the absence of external stimulation. This indicates that CF modeling can be used to evaluate cortical processing in participants in which the visual input may be compromised. Furthermore, by using Bayesian CF modelling it is possible to estimate the co-variability of the parameter estimates and therefore, apply CF modeling to single cases. However, no previous studies evaluated the (Bayesian) CF model using 3T resting-state fMRI data. This is important since 3T scanners are much more abundant and more often used in clinical research compared to 7T scanners. Therefore in this study, we investigate whether it is possible to obtain meaningful CF estimates from 3T resting state (RS) fMRI data. To do so, we applied the standard and Bayesian CF modeling approaches on two RS scans, which were separated by the acquisition of visual field mapping data in 12 healthy participants.

Our results show good agreement between RS- and visual field (VF)- based maps using either the standard or Bayesian CF approach. In addition, to quantify the uncertainty associated with each estimate in both RS and VF data, we applied our Bayesian CF framework to provide the underlying marginal distribution of the CF parameters. Finally, we show how an additional CF parameter, *beta*, can be used as a data-driven threshold on the RS data to further improve CF estimates. We conclude that Bayesian CF modeling can characterize local functional connectivity between visual cortical areas from RS data at 3T. Moreover, observations obtained using 3T scanners were qualitatively similar to those reported for 7T. In particular, we expect the ability to assess parameter uncertainty in individual participants will be important for future clinical studies.

Highlights:

- Local functional connectivity between visual cortical areas can be estimated from RS-fMRI data at 3T using both standard CF and Bayesian CF modelling.
- 3T observations were qualitatively similar to those previously reported at 7T.
- Bayesian CF modelling quantifies the model uncertainty associated with each CF parameter on RS and VF data, important in particular for future studies on clinical populations.

3.1 INTRODUCTION

Spontaneous blood-oxygen level dependent (BOLD) fluctuations have been used to study the intrinsic functional connectivity of the human brain. In 1995, Biswal and colleagues observed, for the first time, the presence of bilateral spatial integration, coherent activity and functional connectivity between distant homotopic brain areas, even in the absence of a task (Biswal et al. 1995). Ever since, resting-state fMRI (RS-fMRI or RS) has played a key role in understanding the temporal and spatial interactions of interconnected brain regions. In parallel, various fMRI data-analysis tools have been developed with the aim to describe the functional and neuroanatomical organization of the brain. One of these methods is connective field (CF) modeling (Haak et al. 2013a). CF, also known as the cortico-cortical population receptive field (cc-pRF), modeling allows to describe the response of a population of neurons in the cortex in terms of the activity in another region of the cortex. It translates the concept of the receptive field into the domain of connectivity by assessing the spatial dependency between signals in distinct cortical visual field regions (Haak et al. 2013a). Even though the approach is agnostic to different stimulus configurations, it has thus far been primarily developed and applied in vision research. A previous study by *Gravel et al.* showed that CFs, estimated from RS-fMRI data recorded at a high magnetic field (7T), reflect the visuotopic organization of early visual cortical maps (Gravel et al. 2014). This indicates that even in the absence of any visual stimulation, CF modeling is able to describe the activity of voxels in a target region (e.g. V2 or V3) as a function of the aggregate activity in a source cortical visual area (e.g. V1).

While these previous results were obtained at 7T and in healthy participants, 3T scanners are much more common, and generally preferred for whole-brain analyses in patient studies (Kolk et al. 2013; Polimeni and Uludağ 2018). Therefore, if RS data recorded at 3T can provide sufficient sensitivity to estimate the spatial integration and connectivity of BOLD signals in distinct regions of the early visual cortex (Gravel et al. 2020), this would open up the CF modeling approach to clinical studies performed at 3T and in individual cases. Amongst others, this would provide the important advantage that plasticity of visual cortical areas could be studied without a dependence on actual visual stimulation. This is important, as in ophthalmic and neurological patients visual input can already be disrupted, potentially resulting in spurious plasticity estimates (H. A. Baseler, Morland, and Wandell 1999; Azzopardi and Cowey 2001; Haak et al. 2013a; Carvalho et al. 2020).

In order to assess the suitability of the CF approach for studying unique patient cases at 3T, we will look beyond the classical variance explained as an indicator of modeling performance. To do so, we will assess the uncertainty of model parameter estimates

using a Bayesian approach. These parameters are available to us by applying our recently developed Bayesian framework for the CF model (Bayesian CF, Invernizzi et al. 2020). In particular, this approach allows to estimate the variability for each CF parameter estimate such as CF size and beta. Moreover, when using our new Bayesian CF framework, we can obtain a data-driven threshold in order to select relevant voxels for both RS-fMRI and visual field mapping (VFM) data.

We applied both the standard CF estimation and the novel Bayesian approach to RS and VFM data acquired at 3T. Subsequently, we compared the CF maps and parameters obtained using the two CF approaches. Additionally, we assessed test-retest reliability between the two runs of RS data.

Finally, we will qualitatively compare our results to those obtained previously in Gravel *et al.*

To preview our results, we found a good agreement between RS- and visual field (VF) -based maps obtained with both the standard and Bayesian CF approach at 3T. Moreover, most observations were qualitatively similar to those previously observed for 7T data. This implies that local functional connectivity between visual cortical areas during RS can be estimated at 3T. No significant differences were found between the two runs of RS data on V1>V2 areas. Furthermore, we showed how the parameter uncertainty can be used to assess the variability of parameters in RS-fMRI BOLD fluctuations. Therefore, the Bayesian CF approach presented here extends on previous approaches to provide an interpretable and independent measure of uncertainty in RS-based data. Finally, we show that the novel retained CF parameter, *beta*, can serve as a sensitive threshold for the selection of voxels and improve the reliability of estimates. Taken together, our results demonstrate the utility of applying a Bayesian CF approach to study inter areal cortical integration in the human visual cortex in health and disease.

3.2 METHODS

3.2.1 Participants

Twelve healthy female participants (mean age 22 years, s.d. = 1.8 years) with normal or corrected-to-normal vision and without a history of neurological disease were included. These data had been collected and used in previous projects (Halbertsma, Haak, and Cornelissen 2019; Invernizzi et al. 2020). For each of the previous studies, the ethics board of the University Medical Center Groningen (UMCG) approved the study protocol. All participants provided written informed consent. The study followed the tenets of the Declaration of Helsinki.

3.2.2 Stimuli presentation and description

The visual stimuli were displayed on a MR compatible screen located at the head-end of the MRI scanner with a viewing distance of 118 cm. The participant viewed the complete screen through a mirror placed at 11 cm from the eyes supported by the 32-channel SENSE head coil. Screen size was 36 x 23 degrees of visual angle and the distance from the participant's eyes to the screen was approximately 75 cm. Stimuli were generated and displayed using the Psychtoolbox (https://github.com/Psychtoolbox-3/Psychtoolbox-3/) and VISTADISP toolbox (VISTA Lab, Stanford University), both MatLab based (Brainard 1997; Pelli 1997). The stimulus consisted of drifting bar apertures (of 10.2 deg radius) with a high contrast checkerboard texture on a grey (mean luminance) background. A sequence of eight different bar apertures with four different bar orientations (horizontal, vertical and diagonal orientations), two opposite motion directions and four periods of mean-luminance presentations completed the stimulus presentation that lasted 192 second. To maintain stable fixation, participants were instructed to focus on a small colored dot present in the center of the screen and press a button as soon as the dot changed color. The complete visual field mapping paradigm was presented to the participant six times, during six separate scans.

3.2.3 Resting state

During the RS-fMRI scans, the stimuli were replaced by a black monitor and the lights in the scanning room were turned off. All participants were instructed to keep their eyes closed, remain as still as possible, not to fall asleep and try not to think of anything in particular.

3.2.4 Data acquisition

MRI and fMRI data were obtained using a 3T Philips Intera MRI scanner (Philips, the Netherlands), with a 32-channel head coil. For each subject, a high-resolution T1-weighted three-dimensional structural scan was acquired (TR = 9.00ms, TE = 3.5ms, flip-angle = 8, acquisition matrix = 251*251*170mm, field of view = 256x170x232, voxel size = 1x1x1mm). Then, six retinotopy (VFM) functional T2*-weighted, 2D echo planar images were obtained (TR = 1500ms, field of view = 224x72x193.5 mm, voxel resolution of 2.33x2.33x3 mm). Finally two, full brain, resting-state (RS) functional T2*-weighted, 2D echo planar images were obtained using the following parameters: TR = 2000ms, field of view = 220x121x220 mm, voxel size = 3.44x3.44x3.29 mm. The functional scans were acquired in the following order: (1) a RS-fMRI scan (RS1) lasted 708s with a total of 350 volumes; (2) six VFM functionals scans were collected, where each scan lasted for 204s with a total of 136 volumes; (3) finally, a second RS-fMRI scan (RS2) with the same characteristic of RS1 (duration of 708s with 350 volumes) was collected. MRI protocol differences between VFM and RS scans are due to the fact

that RS was collected at whole-brain while VFM scans were geared to the visual areas in the occipital brain areas.

Prior to the first VFM scan, a short T1-weighted anatomical scan with the same field of view chosen for the functional scans were acquired and used for obtaining a better co-registration between functional and anatomical volume.

3.2.5 Data analysis

Preprocessing and standard CF analysis of fMRI data were done using ITKGray (http://www.itk.org), Freesurfer (Fischl 2012) and mrVista toolbox for Matlab environment (VISTASOFT, http://vistalab.stanford.edu/). The Bayesian pRF and CF approaches were developed and implemented in MatLab 2016b (The Mathworks Inc., Natick, Massachusetts). The code for the Bayesian pRF and CF frameworks will be made available via www.visualneuroscience.nl.

For each participant, the structural scan was aligned in a common space defined using the anterior commissure-posterior commissure line (AC-PC line) as reference. Next, grey and white matter were automatically segmented using Freesurfer and manually adjusted using ITKGray (http://itk.org), in order to minimize segmentation errors. Then, all functional data were pre-processed using mrVista toolbox. For both RS and retinotopy data the following steps are applied. First, head motion within and between scans were corrected by using robust multiresolution alignment of MRI brain volumes (Nestares and Heeger 2000) an alignment of functional data into anatomical space and an interpolation of functional data with segmented anatomical grey and white matter. For RS-fMRI data, a few additional denoised steps were applied. These steps were possible since RS scans were acquired at the whole brain. First, spatial smoothing of 6mm FWHM was applied in order to perform the denoising step based on ICA-AROMA that identified noise and motion related components (Pruim et al. 2015). These components were then removed from the unsmoothed RS-fMRI data that are now further filtered by applying a band-pass filter with high-pass discrete cosine transform with cut-off frequency of 0.01 Hz and a low-pass 4th order Butterworth filter with cut-off frequency of 0.1 Hz.

3.2.5.1 Bayesian population receptive field mapping applied to VFM

Retinotopy scans were analyzed using a Bayesian population receptive field (pRF) framework. For a detailed account see (Prabhakaran et al. 2020), which uses a Markov Chain Monte Carlo (MCMC) approach to sample the parameter space for the pRF mapping. Following the nomenclature of (Zeidman et al. 2018; Dumoulin and Wandell 2008; Carvalho et al. 2020; Prabhakaran et al. 2020), we defined 2D symmetrical Gaussian kernel centered at x_0, y_0 with width defined as the standard deviation σ, to

define the pRF model. The best model fit was projected onto a smoothed 3D mesh of the cortex. Based on the obtained parameter-values, visual areas are outlined (V1, V2, V3, hV4, LO1 and LO2) to act as source (V1) or target region (all other) for subsequent RS analysis.

3.2.5.2 Standard connective field mapping of RS data

In the standard CF model, the optimal CF parameters (CF position and CF size, which define the 2D symmetric Gaussian kernel) were estimated based on a procedure that fitted the time-series for each location in the target region (e.g. V2 or V3) using a linear combination of the time-series in the source region (e.g. V1; Haak et al. 2013b). The best fitting models are retained and projected on a smoothed 3D mesh. The CF parameters associated with the best fitting model are converted from cortical units (cortical position) into visual field units (eccentricity and polar angle). This is done by inferring the pRF properties — obtained via the Bayesian pRF method Prabhakaran et al. 2020 of the center voxel in the source region for each target location (Haak et al. 2013b).

3.2.5.3 Bayesian connective field mapping

Similar to the Bayesian pRF, the Bayesian CF framework uses a Markov Chain Monte Carlo (MCMC) approach to sample the source region efficiently. Again we used a 2D symmetric Gaussian kernel to predict the time series of the target regions. As in the standard CF modeling, the eccentricity and polar angle values associated with the CF centres are inferred from a pRF mapping. For the sake of completeness, the entire fitting procedure of the Bayesian CF model (option B) is described in the supplementary materials.

For each participant, standard and Bayesian-CF models were estimated for both VFM and RS data. Target and source regions definitions were based on the Bayesian pRF analysis. For both Bayesian pRF and CF models, a total of 15000 iterations were computed, where the first 10% of iterations were discarded for the burn-in process (Liu, Nordman, and Meeker 2016; Chib 2011) and the posterior probability distributions were estimated on the remaining samples.

3.2.5.4 Spatial analysis

We used Pearson and circular correlations to compare and assess the topographic organization of eccentricity and polar angle, respectively, in both standard CF and Bayesian CF maps obtained on RS and VFM data. The same type of correlations were used to evaluate similarities in eccentricity and polar angle maps between the two RS-fMRI scans obtained with standard CF and Bayesian CF models. Furthermore, we computed the coefficient of variation (Shoukri et al. 2008) to evaluate the within-

subject reproducibility of CF parameter estimates obtained by using the standard CF and Bayesian CF. Correlation values higher than 0.5 and p-values below 0.05 were considered statistically significant. Moreover, to compare the relation between CF size and eccentricity RS-based, we binned the eccentricity at 1 degree intervals and applied a linear fit over the mean per bin. A confidence interval (CI) of the fit was defined by applying a bootstrap technique 1000 times.

For the spatial analyses, only voxels for which the best-fitting CF model explained more than 15% of the time-series variance in the standard CF and eccentricity which is < 1deg and > 7deg were included. This arbitrary threshold level was chosen based on previous literature (Baseler et al. 2011; Haak et al. 2013a; Haak, Cornelissen, and Morland 2012; Winawer et al. 2010).

Finally, the intraclass correlation coefficient (ICC) (McGraw and Wong 1996; Perinetti 2018) was computed to estimate the test-retest reliability between the two RS-fMRI scans obtained with standard CF and Bayesian CF models. A priori 5% strongest activated voxels based on VE was used as threshold to compute the ICC score. We also report the relation between ICC and 5 different thresholds (1%, 5%, 10%, 25% and 50%, Supplementary material, Figure 4S).

3.2.5.5 Bayesian analysis

Based on a quantile analysis of the posterior distribution (Invernizzi et al. 2020), we computed a voxel-wise uncertainty measure for each CF parameter by subtracting the upper (Q_3) and lower (Q_1) quantile of the posterior distribution. The estimated uncertainty was computed for both RS and VFM data for each participant and then projected onto a smoothed 3D mesh of the cortex. We repeated the same procedure for each CF parameter.

3.2.5.6 Beta threshold

Following the procedure reported by Invernizzi et al., we test if *beta* – the scaling amplitude of the predictor to the amplitude of the measured signal – can serve as data-driven threshold for RS-data. As a proxy distribution for the null hypothesis (i.e. no correlation between source and target region), one surrogate BOLD time series was calculated for each voxel (Räth and Monetti 2009; Schreiber and Schmitz 1996; Lancaster et al., 2018). A surrogate time series was generated using the iterative amplitude adjusted Fourier transform method (iAAFT, Räth and Monetti 2009; Schreiber and Schmitz 1996). Then, the Bayesian CF model was fitted using this surrogate to real time series of the target region which were unchanged. Based on the best fit obtained in the MCMC iterations of the surrogate *beta*-estimate, we calculated a familywise error (FWE) corrected *beta*-threshold for all the voxels in the target region. Based on

previous literature, we selected the cut-off value of the 95th percentile (Bornmann 2013; Invernizzi et al. 2020) of the null distribution as FWE-corrected *beta* threshold. Finally, we compared the voxel selection at the single participant level using VE and the FWE *beta*-threshold approaches.

3.3 RESULTS

The CF maps obtained from RS-based data for eccentricity, polar angle and CF size were qualitatively comparable for the standard and Bayesian CF models. In contrast to the VFM data, the relation with CF size and eccentricity in RS data does not increase with visual hierarchy. Again, the same behaviour was observed using both methods. No statistically significant difference was found between the two RS scans for any CF parameter. We estimated the uncertainty for the Bayesian CF parameters (CF size and beta). An higher uncertainty from the CF parameters was observed from both RS scans compared to VFM data and between RS2 and RS1 scans. Finally, we showed how to use a new threshold based on the effect size of the model both in the presence and absence of visual stimuli.

3.3.1 CF models based on RS-fMRI data

We used V1 as source region while V2, V3, hV4, LO1 and LO2 as target to derive CF maps projected on a smoothed 3D mesh on a single subject level (Figure 1). Such maps were created using both standard CF and Bayesian CF models (Figure 1, panel B, C, D, and E). Topographical maps for eccentricity, polar angle and CF size were comparable for both CF models using RS data (Figure 1). We used the VFM-based maps as reference (Figure 1, Panel A) as these maps show a clear visuotopic organization for all the CF parameters estimated. Then the same parameters are plotted for all RS scans (Figure 1 - Panel B and D: RS-based derived maps using standard CF model; Panel C and E: RS-based derived maps using Bayesian CF model). Furthermore, a good level of within-subject reproducibility was observed for each CF parameter estimate for both CF models using RS scans (supplementary material, Table S2).

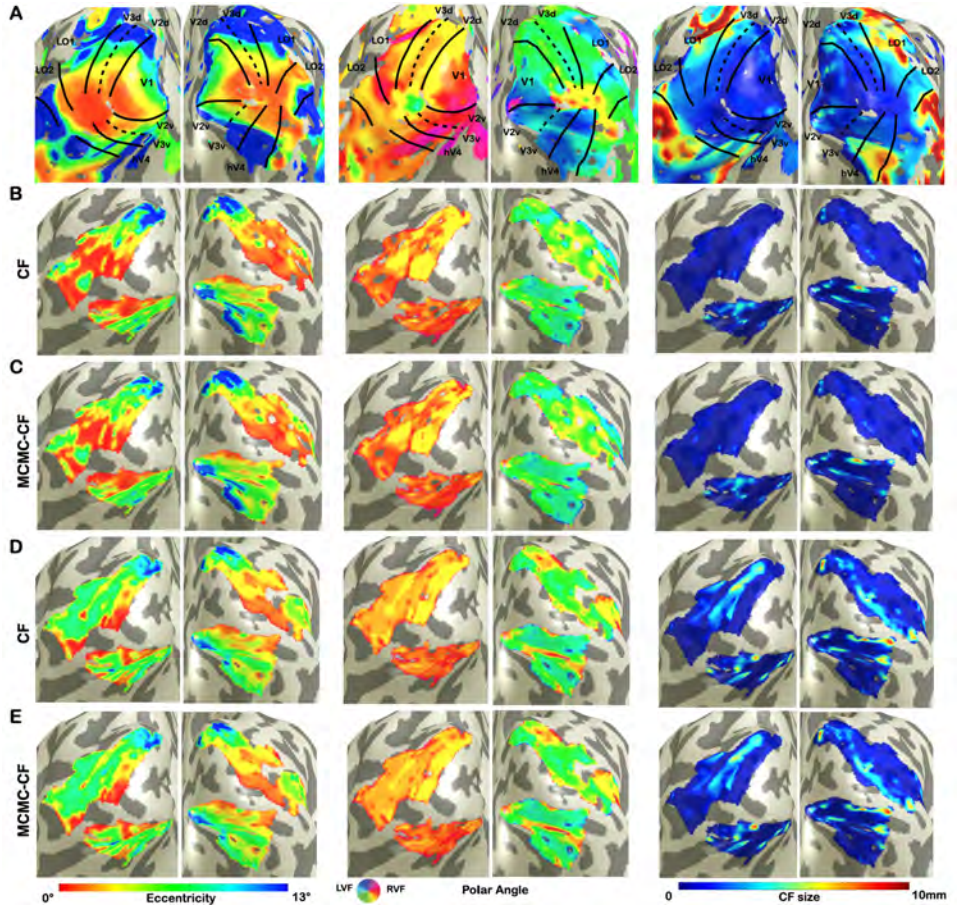

Figure 1 - Visualization of CF maps of denoised data for a single participant. From left to right: eccentricity, polar angle and CF size. Panel A corresponds to VFM derived estimates. Panels B and C show parameter estimates for the first RS run (RS1) using standard CF and Bayesian CF models, respectively. Panels D and E show parameter estimates for the second RS run (RS2) using standard CF and Bayesian CF models, respectively. The fact that panels B and C on the one hand, and D and E on the other, are very comparable is important and indicates that the standard and Bayesian CF models produce highly similar results on RS data.

In line with the earlier work that introduced the standard CF method (K. V. Haak, Morland, and Cornelissen 2013), we quantified possible differences between the resulting RS-based CF and Bayesian-CF estimates by correlating them against the pRF-derived eccentricity and polar angle parameters that we used as reference (Table 1). Eccentricity and polar angle parameters are estimated for each single participant and then concatenated across participants to calculate the Spearman's correlation and circular correlation, respectively. Overall a good agreement was found for V1 >

V2 and V1>V3 areas using both CF models. Negative or almost zero correlation values can be observed for CF estimates between distant visual areas (i.e. V1>LO1, V1>LO2).

To check the possible influence of the denoise procedure applied to RS data, the same quantification analysis was computed on non-denoised RS data. Similar results were observed indicating that the ICA-AROMA denoise procedure on RS-fMRI data did not influence the final CF outcomes. A complete overview of these analyses is reported in supplementary material (Figure S1 and Table S1).

Eccentricity									
ROIs	Standard CF versus pRF								
	VFM			RS1			RS2		
	r	IQR [Q1,Q3]	p-value	r	IQR [Q1,Q3]	p-value	r	IQR [Q1,Q3]	p-value
V1 --> V2	0.86	[0.82, 0.91]	p<0.001	0.44	[0.38, 0.54]	p<0.001	0.57	[0.47, 0.62]	p<0.001
V1 --> V3	0.82	[0.76, 0.87]	p<0.001	0.22	[0.13, 0.34]	p<0.001	0.31	[0.17, 0.43]	p<0.001
V1 -> hV4	0.81	[0.73, 0.83]	p<0.001	0.02	[-0.09, 0.40]	0.0048	0.34	[0.04, 0.46]	p<0.001
V1 -> LO1	0.78	[0.72, 0.81]	p<0.001	0.07	[-0.13, 0.24]	0.0018	0.15	[0.04, 0.3]	0.0021
V1 -> LO2	0.63	[0.43,0.75]	p<0.001	-0.06	[-0.27, 0.17]	0.0154	0.08	[-0.04, 0.27]	0.0567
ROIs	Bayesian CF versus pRF								
	VFM			RS1			RS2		
	r	IQR [Q1,Q3]	p-value	r	IQR [Q1,Q3]	p-value	r	IQR [Q1,Q3]	p-value
V1 --> V2	0.86	[0.82, 0.91]	p<0.001	0.48	[0.34, 0.57]	p<0.001	0.58	[0.51, 0.63]	p<0.001
V1 --> V3	0.82	[0.77, 0.87]	p<0.001	0.25	[0.09, 0.43]	p<0.001	0.3	[0.16, 0.41]	p<0.001
V1 -> hV4	0.79	[0.73, 0.84]	p<0.001	0.08	[-0.16, 0.35]	0.0085	0.28	[0.06, 0.40]	p<0.001
V1 -> LO1	0.78	[0.72, 0.82]	p<0.001	0	[-0.17, 0.28]	0.0667	0.24	[0.10 0.43]	p<0.001
V1 -> LO2	0.65	[0.54, 0.76]	p<0.001	-0.03	[-0.25, 0.18]	0.0641	0.09	[-0.02, 0.38]	0.2264
Polar Angle									
ROIs	Standard CF versus pRF								
	VFM			RS1			RS2		
	r	IQR [Q1,Q3]	p-value	r	IQR [Q1,Q3]	p-value	r	IQR [Q1,Q3]	p-value
V1 --> V2	0.92	[0.85,0.93]	p<0.001	0.64	[0.41, 0.82]	p<0.001	0.78	[0.178, 0.84]	p<0.001
V1 --> V3	0.84	[0.78, 0.89]	p<0.001	0.17	[-0.05, 0.82]	0.002	0.26	[-0.53, 0.49]	p<0.001
V1 -> hV4	0.79	[0.51, 0.92]	p<0.001	-0.29	[-0.62, 0.66]	p<0.001	0.54	[-0.31, 0.77]	p<0.001
V1 -> LO1	0.79	[0.55, 0.89]	p<0.001	0.68	[0.34, 0.76]	p<0.001	0.56	[-0.11, 0.72]	p<0.001
V1 -> LO2	0.72	[0.46, 0.76]	p<0.001	0.49	[-0.23, 0.68]	0.0046	0.62	[-0.46, 0.76]	p<0.001
ROIs	Bayesian CF versus pRF								
	VFM			RS1			RS2		
	r	IQR [Q1,Q3]	p-value	r	IQR [Q1,Q3]	p-value	r	IQR [Q1,Q3]	p-value
V1 --> V2	0.92	[0.87, 0.93]	p<0.001	0.62	[0.40, 0.85]	p<0.001	0.83	[0.39, 0.87]	p<0.001
V1 --> V3	0.84	[0.70, 0.92]	p<0.001	0.17	[-0.03, 0.68]	p<0.001	0.17	[-0.36, 0.48]	p<0.001
V1 -> hV4	0.79	[0.51, 0.92]	p<0.001	-0.34	[-0.55, 0.17]	p<0.001	0.54	[-0.02, 0.71]	p<0.001
V1 -> LO1	0.82	[0.55, 0.90]	p<0.001	0.35	[0.10, 0.64]	0.0045	0.52	[-0.08, 0.79]	p<0.001
V1 -> LO2	0.67	[0.51, 0.82]	p<0.001	0.24	[-0.22, 0.76]	0.0021	0.3	[-0.35, 0.83]	p<0.001

Table 1 - Group level correlation between visual field and resting state maps derived using Bayesian pRF and CF modeling. Correlations coefficients were computed in order to assess the level of agreement between the eccentricity (Pearson's correlation) and polar angle (circular correlation) estimates obtained by using standard CF and Bayesian CF models and the ones derived by the pRF. We used the VFM-based pRF estimates as reference as stimuli driven and they further show a clear visuotopic organization for all parameters. Correlation, p-values and interquartile range values were estimated at single subject level and then concatenated across all participants.

3.3.2 Test-retest reliability

To estimate test-retest reliability between the two RS scans, we selected the 5% most active voxels and computed the ICC score for each parameter estimate obtained using both CF and Bayesian CF model. For completeness, the relation between ICC and chosen threshold is displayed in figure 4S. A positive ICC value is reported for V1>V2 using both models. For higher order visual areas this ICC value gradually drops for all parameters.

Table 2 - Test-retest evaluation between RS scans.

Eccentricity				
ROIs	CF standard		Bayesian CF	
	ICC (r)	IQR [Q1, Q3]	ICC (r)	IQR [Q1, Q3]
V1 --> V2	0.9661	[0.943, 0.983]	0.9061	[0.844, 0.948]
V1 --> V3	0.2072	[0.073,0.462]	0.193	[0.074, 0.313]
V1 -> hV4	0.1045	[-0.012, 0.426]	-0.006	[-0.065, 0.503]
V1 -> LO1	0.0909	[-0.109, 0.343]	-0.0194	[-0.225, 0.235]
V1 -> LO2	0.1036	[-0.184, 0.604]	0.0413	[-0.244, 0.221]
Polar Angle				
ROIs	CF standard		Bayesian CF	
	ICC (r)	IQR [Q1, Q3]	ICC (r)	IQR [Q1, Q3]
V1 --> V2	0.9295	[0.874, 0.976]	0.8717	[0.720, 0.941]
V1 --> V3	0.3365	[0.179, 0.495]	0.2997	[0.075, 0.463]
V1 -> hV4	-0.027	[-0.081, 0.157]	-0.0583	[-0.209, 0.067]
V1 -> LO1	0.0732	[-0.106, 0.536]	0.1944	[-0.053, 0.48]
V1 -> LO2	0.4057	[0.137, 0.734]	0.2635	[0.064, 0.6036]
CF size				
ROIs	CF standard		Bayesian CF	
	ICC (r)	IQR [Q1, Q3]	ICC (r)	IQR [Q1, Q3]
V1 --> V2	0.2939	[0.168, 0.396]	0.2192	[0.061, 0.344]
V1 --> V3	0.0214	[-0.029, 0.139]	0.0335	[-0.077, 0.201]
V1 -> hV4	-0.0533	[-0.131, 0.147]	0.0717	[-0.042, 0.156]
V1 -> LO1	-0.0308	[-0.153, 0.049]	-0.0292	[-0.166, 0.076]
V1 -> LO2	-0.075	[-0.144, -0.017]	-0.1147	[-0.141, -0.007]

For eccentricity, polar angle and CF size estimates obtained by using the standard CF and the Bayesian CF models. Intraclass correlation coefficients (ICC) were computed across all participants and for each roi separately. Median and interquartile range are computed across the group.

3.3.3 Assessing uncertainty in RS-fMRI data

In order to estimate a voxel-wise uncertainty value associated to each CF parameter, we computed a quantile analysis of the posterior distribution for each participant. Then, for illustrative purposes, we projected on a smoothed 3D mesh the uncertainty estimates obtained for a single participant (Figure 2), where V1 is the source region

and V2, V3, hV4, LO1, and LO2 were the target regions; VFM-based CF maps were used as reference (Fig. 2*A*). An increased uncertainty in beta estimate in RS1- and RS2-based CF maps was observed compared to VFM-based CF maps but not for CF size. Interestingly, no clear uncertainty-related visuotopic organization was found either for VFM or RS data. Furthermore, we evaluated the possible dependency between the Bayesian parameter estimates and the corresponding (posterior) uncertainty by computing the cross-correlation coefficient between these estimates (Table 3). In line with the findings reported in (Bornmann 2013; Invernizzi et al. 2020) for VFM data, a weak correlation exists between beta, sigma parameter estimates and their respective uncertainties obtained on RS-data (Table 3). Again, this indicates that uncertainty is an additional, independent parameter, but this time obtained from resting-state data. The uncertainty CF maps derived from two additional participants are reported in supplementary material (Figure S5).

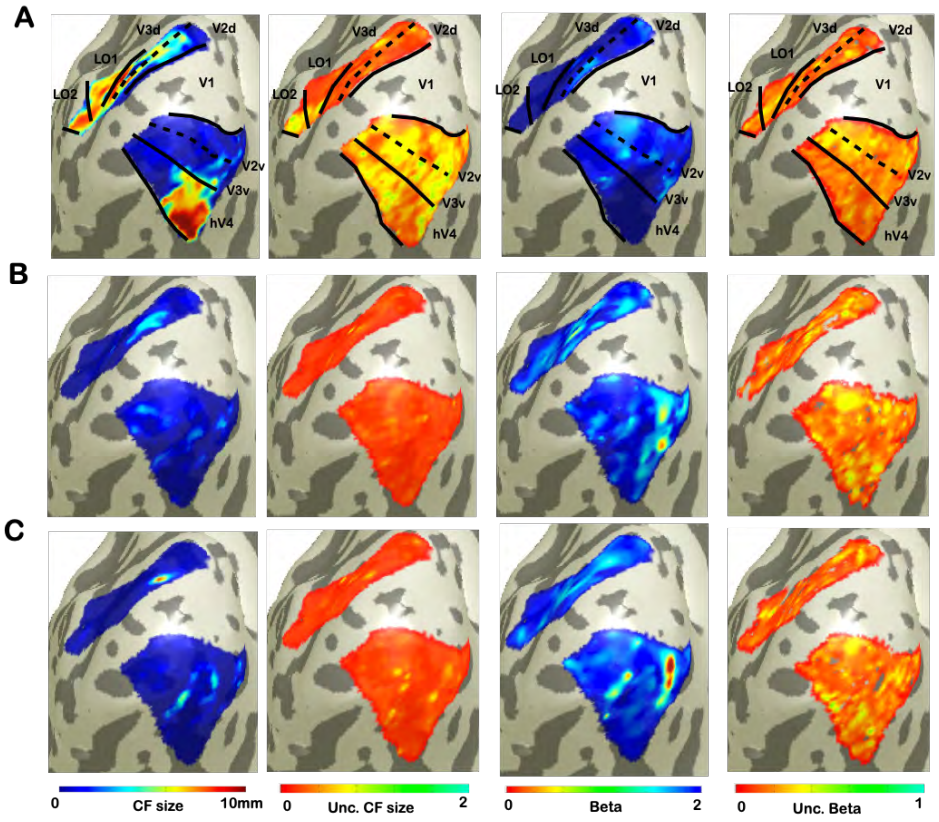

Figure 2 - Visualization of uncertainty for CF parameter at single participant. From left to right: CF size, uncertainty of CF size, beta, and uncertainty of beta. Panel A corresponds to VFM derived estimates. While, bottom panels B and C show the parameters and uncertainty estimates for each of the two RS scans.

Table 3 - Dependency between Bayesian CF parameters and uncertainties for both RS scan at group level.

	V1 > V2		V1 > V3		V1 > hV4		V1 > LO1		V1 > LO2	
RS1	*CF size*	*Beta*	*CF size*	*Beta*	*CF size*	*Beta*	*CF size*	*Beta*	*CF size*	*Beta*
Unc. CF size	0.06	-0.01	0.11	0.04	0.1	0.07	0.15	0.1	0.1	0.09
Unc. Beta	-0.03	0.01	-0.01	0.01	-0.04	0.01	-0.03	-0.12	-0.01	-0.01
RS2	*CF size*	*Beta*	*CF size*	*Beta*	*CF size*	*Beta*	*CF size*	*Beta*	*CF size*	*Beta*
Unc. CF size	0.08	-0.08	0.06	-0.05	0.04	-0.02	0.03	0.02	-0.02	-0.06
Unc. Beta	0.01	-0.01	0.01	-0.02	0.01	-0.03	-0.03	-0.04	-0.02	0.04

Cross-correlations were computed between the estimated Bayesian CF parameters and the uncertainty derived from them. Only the CF parameters directly estimated using the model (CF size and beta) are included in this analysis. CF size, beta and their associated uncertainties were estimated at single participant level and then concatenated across all participants.

3.3.4 Bayesian CF thresholding application

To evaluate the goodness of the corrected beta-thresholding method in the voxel selection on RS data, we compared the model VE, each CF parameter and the uncertainty associated, respectively (Figure 4, CF size and Figure 2S, beta parameter). Both thresholds: VE is higher than 15% and the FWE corrected effect size (>95% Figure 4, Panel A; for more details, see (Invernizzi et al. 2020) are indicated. Based on a direct comparison of FWE *beta*-corrected threshold (CI) to the standard VE of the model (Figure 4, Panel B and C), the 95% FWE CI-based threshold proved to be more conservative. Note that it is not straightforward to identify a point at which the two threshold definitions will be equivalent.

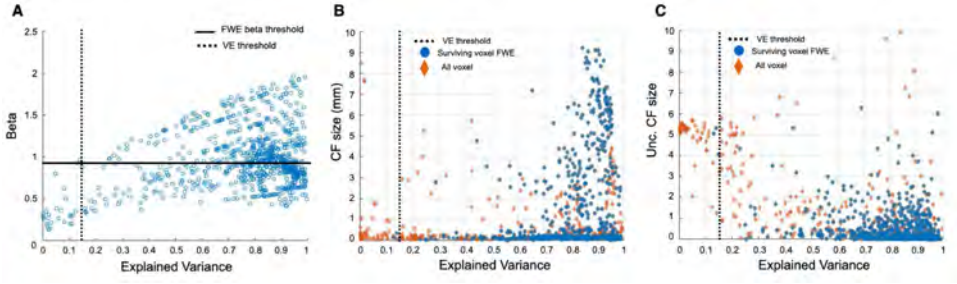

Figure 4 - Comparison of thresholding approaches at a single participant level for V1>V2 connectivity based on RS1 data.
In Panel **A,** the FWE *beta*-corrected thresholds obtained with both 95% CI and the standard VE of the model are shown. A direct comparison between the FWE threshold and the standard VE is presented in Panels B and C. Since we are interested in testing this FWE-corrected threshold in different conditions, CF size ~0 which are discarded. In Panel **B**, the relation between VE and the Bayesian CF size is presented for all voxels (orange diamonds). Blue dots indicate the voxels surviving the 95% CI FWE beta-threshold. The standard VE threshold is not applied but indicated by a black dotted line. In Panel **C**, the relation between VE and the uncertainty associated with the CF size is presented. Note that high uncertainty can be associated with voxels with a high VE.

This threshold was then used to compare the relation between RS-based CF size and VFM-derived eccentricity. Figure 5 shows that RS-based CF size does not increase with eccentricity within the early visual areas. While it is possible to notice an increase of CF size values with eccentricity only for the later visual areas (LO1 and LO2), especially in RS2. However, no significant differences were found between RS1 and RS2 scans in areas along the visual hierarchy.

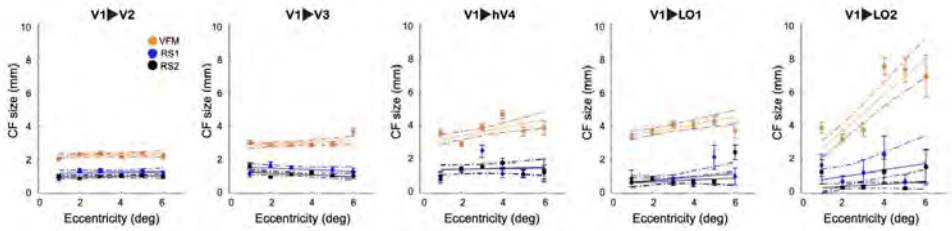

Figure 5 - Connective field size as a function of VFM- based eccentricity for RS and VFM scans. For both RS and VFM scans, eccentricity was binned in intervals of 1 deg and a linear fit was applied. The average CF size was calculated only for voxels that survived the FWE 95%CI threshold. Each dot indicates the mean of the CF size in each bin. The dashed lines correspond to the 95% bootstrap confidence interval of the linear fit. For reference, the VFM data is included.

3.4 DISCUSSION

In this study, we show that 3T RS-fMRI data is suitable for estimating local functional connectivity between visual cortical areas. Furthermore, we observed a good level of agreement between the standard and Bayesian (MCMC) CF models. This indicates that also the latter tool is suitable for studying the cortico-cortical properties of brains at rest. The obtained CF estimates are qualitatively similar to those previously observed for 7T RS-fMRI data. This further supports that sensitive estimations and associated uncertainties can be derived from 3T RS-fMRI data. Finally, we show that a FWE-corrected threshold can be used as a complementary threshold to the standard VE to increase the reliability of estimates. This indicates that both stimulus-driven and RS-based CF modeling are suitable approaches for use in patient- or single-case studies. Below, we discuss our findings in more detail.

3.4.1 Comparable CF estimates based on resting-state and visual field mapping at 3T fMRI

The CF method was previously used to reveal relevant aspects of resting-state brain activity using high-resolution 7T-fMRI. Crucially, in this study, we have extended the CF approach and assessed its performance at a lower-field strength (3T-fMRI). Higher magnetic fields can increase the signal-to-noise ratio, the tissue specificity and the

spatial resolution of fMRI recordings. However, 3T scanners are much more abundant and more often used in clinical research than 7T ones. Our present findings indicate that, despite the limited resolution of metabolism-sensitive measurements such as fMRI for determining the contribution of neuronal activity to hemodynamic signals, it is still possible to study the aggregate neuronal population properties at 3T using CF approaches. A good level of agreement was found between the CF and Bayesian CF maps estimated from RS and those estimated based on VFM for all CF parameters in the early visual areas (Figure 1 and table 1 - V1>V2, V1>V3). Our quantitative and qualitative results are in agreement with those presented previously (Haak et al. 2013a; Gravel et al. 2014; Invernizzi et al. 2020). Qualitatively, we find that the CF maps obtained at 3T are in fair agreement to those obtained at 7T (Gravel et.al, 2014, Figure 3). Moreover, while we observed variability in the CF maps estimated for different RS scans, this was also observed previously at 7T (Gravel et al. (2014).

Thus, RS-derived CF maps at least partly reflect the functional topographic organization revealed by pRF mapping – regardless of the lower spatial resolution and signal-to-noise ratio afforded by 3T-fMRI. While higher magnetic field strengths allow for an enhanced spatiotemporal resolution, the temporal resolution of fMRI is limited by the hemodynamic response to neuronal activity, not by the magnetic field strength. This suggests that the spatially-weighted temporal correlations, as captured by the CF method, suffice to reveal the underlying retinotopically organized connectivity between areas.

Examining the relationship between CF size and pRF eccentricity revealed that RS-derived CF size did not increase with eccentricity, neither within individual areas nor throughout the visual hierarchy (Figure 2 and Figure 5). In contrast, for VFM, we did find increased CF sizes at higher pRF eccentricities (Fig. S3, supplementary material). This was most pronounced for higher-order visual area LO2. The same trend was observed in previous results obtained at 7T (Gravel et al. 2014).

In addition, we investigated whether spatial structure could be observed in the uncertainty information, which could potentially be due to large-scale network interactions, physiological processes or measurement noise. In order to do so, we compared the uncertainties associated with CF size, effect size (beta) in the different conditions (Figure 3; Table 3). However, neither in the VFM nor in the RS based uncertainty maps did we observe a clear visuotopic organization (Figure 3). Moreover, for the RS data, we find only weak correlations between the CF size and beta and their corresponding uncertainties (correlation < 0.25). This is similar to what we observed previously for VFM data (Invernizzi et al. 2020). Therefore, we conclude that, given these rather weak (co)dependencies, the uncertainties can be treated as additional and

independent CF parameters describing the RS state data.

3.4.2 The effect size as a new approach for voxel-wise thresholding of RS data

The Bayesian variant of CF modeling, in addition to the uncertainties for the CF parameters, provides also a parameter beta describing effect size (β). This parameter can be used to threshold data in a voxel-wise manner similar to the estimated Variance Explained (VE). Since VE indicates the goodness of fit for the model, the current standard approach is to threshold voxels based on the VE of the model for both VFM and RS data (Haak et al. 2013a; Gravel et al. 2014; Halbertsma, Haak, and Cornelissen 2019). However, a high VE does not always correspond to a low uncertainty in the parameter estimates (Thielen et al. 2019). As previously shown for VFM data, beta thresholding provides an alternative thresholding approach (Invernizzi et al. , 2020). Here, we show that a FWE-corrected *beta* threshold based on the 95% CI also provides a valid approach for RS data and compares favourably to VE thresholding (Figure 4 and 2S). However, some thought should be given before applying it to RS data. On the one hand, *beta* thresholding is more sensitive in the selection of voxels compared to the standard VE. Given that RS data is inherently more noisy than VFM data and this might affect the applicability of *beta*-thresholding for this type of scan. On the other hand, a marked advantage of the FWE *beta*-thresholding approach is that it is participant-specific (Invernizzi et al. 2020). Therefore, using it ensures minimizing the loss of individual participant data and is expected to be especially useful when the Bayesian CF framework is applied to RS data acquired in clinical populations (e.g. with a lesioned visual pathway or brain neurodegeneration). In general, we conclude that FWE *beta*-thresholding is a useful complementary approach to the standard VE thresholding for both VFM and RS data.

3.4.3 Relationship between resting state signals and functional architecture.

Recent studies have shown that indirect measures of intrinsic neuronal activity, such as spontaneous BOLD fluctuations recorded during RS, can still reflect the organization of the neuroanatomical connectivity that characterizes early visual cortical areas. These studies have allowed the assessment of both fine-grained within- and between-area interactions. This observed spatial specificity in spontaneous BOLD fluctuations can only emerge if these are anchored in the topographically organized architecture of the visual system, as has been shown on multiple occasions (H. A. Baseler, Morland, and Wandell 1999; Azzopardi and Cowey 2001; Haak et al. 2013a; Biswal et al. 1995). However, the neuronal and physiological basis of these BOLD patterns is still unclear. Whether spontaneous fMRI activity reflects the consequences of local population spiking activity, sub-threshold neuronal activity (N. K. Logothetis et al. 2001; Shi et al. 2017), or metabolic relationships between neurons and astrocytes (e.g. neuro-vascular coupling) is still a matter of debate (O'Herron et al. 2016; Pang et al. 2017). It is possible

that retinotopically organized inter-areal BOLD coupling patterns reflect intrinsic activity in distant cortical areas, sharing similar selectivity in visual field positions which is likely due to "hard wired", i.e. white matter bundle coupling. Alternatively, these patterns may reflect the footprint of slow fluctuations that traverse the brain like "waves" (Logothetis et al. 2004; Carandini et al. 2015). Recent studies have unified these contrasting views by showing that both global fluctuations, in the form of propagating hemodynamic waves, and transient local coactivations are necessary for setting the spatial structure of hemodynamic functional connectivity (Matsui, Murakami, and Ohki 2016; Pisauro et al. 2013). Taken together, these studies point to the multiple roles that neuroanatomical, physiological and vascular factors play in shaping spontaneous RS activity in a way that gives rise to visuotopically organized fluctuations in the BOLD signal. The similar visual field position selectivity revealed by RS- and VFM-derived CF maps, suggest a shared neuroanatomical origin.

3.4.4 Limitations and future directions

Here, we qualitatively compared local functional connectivity at different magnetic field strengths obtained in different participants. For a direct comparison, the 3T and 7T derived results should ideally be obtained in the same participants. However, in our view, the differences in the acquisition protocols are minor and there is no reason to burden a new cohort of participants to obtain new scans. Nevertheless, while we indeed report a good level of agreement between the CF estimates obtained using the RS and VFM scans, future studies should consider using identical MR parameters for the VFM and RS scans. Moreover, such future studies could investigate the correlations in the temporal and spatial domain in the cortex extending the Bayesian CF model to capture distinct dynamics in functional connectivity, and their relationship to different cognitive and behavioural states, both in health and disease. Furthermore, such studies could also consider the influence of high frequency fluctuations (above 0.1 Hz) in the spontaneous BOLD signal (Chen and Glover 2015) on CF parameter estimates. Finally, the stimulus-agnostic and eye-movement independent character of the CF analysis invites applying the present approach also to other cortical regions, such as those involved in auditory, somatosensory, or motor processing (Knapen, 2020).

3.5 CONCLUSION

We have shown that CF modeling is a suitable tool to characterize and quantify the local functional connectivity of visual cortical areas during resting state at 3T. Moreover, the CF modeling at 3T provides qualitatively similar results to those previously observed at 7T, indicating that this lower, yet much more commonly available, field strength would be sufficient for characterizing the brains of patients and individual cases.

Finally, we show that our novel Bayesian CF modeling approach provides additional and independent parameters such as uncertainty and effect size that, in principle, can be used to compare the local functional connectivity over different conditions, models and/or groups and assess the statistical significance of the modeling.

3. SUPPLEMENTARY MATERIAL

S1. Bayesian connective field model

The following description is adapted from Invernizzi et al. (2020).

Based on the CF definition used in the standard approach (Haak et al. 2013b), a linear spatiotemporal model and a 2D symmetric Gaussian connective field model (2) are used to create a predicted time series ($p(t)$) which is fitted to the time series $y(t)$ of a target location (1) .

$$y(t) = p(t)\beta + \varepsilon \quad (1)$$

$$g(v) = exp - [D(v, v_0)^2/2\sigma^2] \quad (2)$$

$$p(t) = \sum_v [a(v,t) * g(v)] \quad (3)$$

Where the predicted fMRI signal $p(t)$ is obtained by the overlap between the CF model $g(v)$ and the neuronal population inputs $a(v,t)$, that are defined as the BOLD time series (converted to percent signal change) for voxels (v) (see eq. 3). In equation 1, β defines the effect size and ϵ is the error term.

The 2D symmetric Gaussian CF model of voxel (v), $g(v)$ is defined based on the shortest three-dimensional distance $D(v, v_0)$ between a voxel (v) and the proposed CF center (v_0) on a triangular mesh representation and σ, which defines the width of the CF. D is computed using Dijkstra's algorithm (Dijkstra 1959) while σ is constrained to the range $[r_0\ r]$ using a latent variable l_σ (Zeidman et al. 2018). A flat prior is assumed for σ. Therefore, the prior for the latent variable l_σ is defined as a normal distribution $N(0,1)$ (see equation 4). As explained in Zeidman et al.(Zeidman et al. 2018), each latent variable is assigned to a prior distribution that represents our beliefs for that CF parameter, before the model fitting.

$$\sigma = (r - r_0) * NCDF(l_\sigma,0,1) + r_0 \quad (4)$$

Where r is the maximum radius and r_0 is the smallest allowed radius for the CF width - that can be an arbitrarily small non-zero number, which here were set to 10.5° and 0.01°, respectively. $NCDF$ indicates the normal cumulative distribution function.

The MCMC is an iterative sampling approach. During each iteration the parameters for a new CF are set and the fit is compared against the current one. A new location will be selected using the distance to the current position ($d_{current}$). Based on the distance matrix (D), the maximum step (ms) possible in the source region was defined as half the maximal distance from the the current position ($d_{current}$) (5). Latent variable l_s, is randomly drawn from a normal distribution N(0,1) which results in a flat prior for the step

size ($step$) between 0 and the maximum step [0 ms] (5, 6). The updated sampling position ($v_{0\ proposal}$) is defined as that position for which the distance to the current position is as close as possible to $step$. If multiple locations are found, only one is drawn randomly.

$$ms = max\ (d_{current})\ /2 \quad (5)$$
$$step = |ms * NCDF(l_s,0,1)| \quad (6)$$

Note that for the first iteration the CF center (v_0) was randomly selected from the source region.

Simultaneous with an updated sample location, an updated width for the CF is calculated. The $l_{\sigma\ proposal}$ is drawn from a gaussian distribution centered around the current value with a width $w_{proposal}$ (7).

$$l_{\sigma\ proposal} = N(l_\sigma, w_{proposal}) \quad (7)$$

The effect size (β) is estimated in parallel to the other CF parameters and constrained to be positive (Zeidman et al. 2018) using the following equation:

$$\beta = exp(l_\beta) \quad (8)$$

A latent variable l_β was defined with a prior distribution $N(-2,5)$ and the next β value was controlled by $l_{\beta\ proposal}$ (9).

$$l_{\beta\ proposal} = N(l_\beta, w_{proposal}) \quad (9)$$

In this study, the initial values of l_σ, l_β and $w_{proposal}$ were set to 1 , -5 and 2, respectively. At each iteration of the MCMC, the updated CF parameters (σ, β) were estimated using the following steps. First a predicted fMRI signal $p(t)$ is generated from the source region using eq 2. Note that $g(t)$ was scaled to ensure that the total area under the gaussian, as calculated across the full source region, was equal to one. Second, the error per time point e_t between the measured fMRI signal ($y(t)$) and the predicted fMRI signal $p(t)$ was calculated. e_t is calculated via subtraction of the predicted signal $p(t)$ from the measured fMRI signal. Then, the log-likelihood L_t associated with e_t was estimated using equation (10). We assumed that e_t follows a standard normal distribution: $N(0,1)$. After estimating the mean and standard deviation of ϵ ($\widehat{\mu_\epsilon}$ and $\widehat{\sigma_\epsilon}$), we calculated the maximum likelihood estimates (MLE, eq. 11).

$$L_t = log(N(-|e_t|, \widehat{\mu_\epsilon}, \widehat{\sigma_\epsilon})) \quad (10)$$
$$MLE = \sum_t L_t + log(N(l_\sigma,0,1)) + log(N(l_\beta,-2,5)) \quad (11)$$

At this point, MLE of the proposal iteration is compared to the last accepted (current) sample based on an Accepted ratio score Ar (12).

$$Ar = exp\ (MLE_{t\ proposal} - MLE_{t\ current}) \qquad (12)$$

Ar was compared to a pseudo-random acceptance score defined as a normal distribution $N(0,1)$ and only if the Ar was higher, the respective latent variables were updated. Based on the accepted l_σ, l_s and l_β values, a new CF was defined and a new MCMC iteration took place.

REFERENCES

Azzopardi, P., and A. Cowey. 2001. "Motion Discrimination in Cortically Blind Patients." *Brain: A Journal of Neurology* 124 (Pt 1): 30–46.

Baseler, H. A., A. B. Morland, and B. A. Wandell. 1999. "Topographic Organization of Human Visual Areas in the Absence of Input from Primary Cortex." *The Journal of Neuroscience: The Official Journal of the Society for Neuroscience* 19 (7): 2619–27.

Baseler, Heidi A., André Gouws, Koen V. Haak, Christopher Racey, Michael D. Crossland, Adnan Tufail, Gary S. Rubin, Frans W. Cornelissen, and Antony B. Morland. 2011. "Large-Scale Remapping of Visual Cortex Is Absent in Adult Humans with Macular Degeneration." *Nature Neuroscience* 14 (5): 649–55.

Biswal, B., F. Z. Yetkin, V. M. Haughton, and J. S. Hyde. 1995. "Functional Connectivity in the Motor Cortex of Resting Human Brain Using Echo-Planar MRI." *Magnetic Resonance in Medicine: Official Journal of the Society of Magnetic Resonance in Medicine / Society of Magnetic Resonance in Medicine* 34 (4): 537–41.

Bornmann, Lutz. 2013. "How to Analyze Percentile Citation Impact Data Meaningfully in Bibliometrics: The Statistical Analysis of Distributions, Percentile Rank Classes, and Top-Cited Papers." *Journal of the American Society for Information Science and Technology*. https://doi.org/10.1002/asi.22792.

Brainard, D. H. 1997. "The Psychophysics Toolbox." *Spatial Vision* 10 (4): 433–36.

Carandini, M., D. Shimaoka, L. F. Rossi, T. K. Sato, A. Benucci, and T. Knopfel. 2015. "Imaging the Awake Visual Cortex with a Genetically Encoded Voltage Indicator." *Journal of Neuroscience*. https://doi.org/10.1523/jneurosci.0594-14.2015.

Carvalho, Joana, Azzurra Invernizzi, Khazar Ahmadi, Michael B. Hoffmann, Remco J. Renken, and Frans W. Cornelissen. 2020. "Micro-Probing Enables Fine-Grained Mapping of Neuronal Populations Using fMRI." *NeuroImage* 209 (April): 116423.

Chen, Jingyuan E., and Gary H. Glover. 2015. "BOLD Fractional Contribution to Resting-State Functional Connectivity above 0.1 Hz." *NeuroImage*. https://doi.org/10.1016/j.neuroimage.2014.12.012.

Chib, Siddhartha. 2011. "Introduction to Simulation and MCMC Methods." *The Oxford Handbook of Bayesian Econometrics*. https://doi.org/10.1093/oxfordhb/9780199559084.013.0006.

Dijkstra, E. W. 1959. "A Note on Two Problems in Connexion with Graphs." *Numerische Mathematik*. https://doi.org/10.1007/bf01386390.

Dumoulin, Serge O., and Brian A. Wandell. 2008. "Population Receptive Field Estimates in Human Visual Cortex." *NeuroImage* 39 (2): 647–60.

Fischl, Bruce. 2012. "FreeSurfer." *NeuroImage* 62 (2): 774–81.

"Foveal pRF Properties in the Visual Cortex Depend on the Extent of Stimulated Visual Field." 2020. *NeuroImage* 222 (November): 117250.

Gravel, Nicolás, Ben Harvey, Barbara Nordhjem, Koen V. Haak, Serge O. Dumoulin, Remco Renken, Branislava Curčić-Blake, and Frans W. Cornelissen. 2014. "Cortical Connective Field Estimates from Resting State fMRI Activity." *Frontiers in Neuroscience* 8 (October): 339.

Gravel, Nicolás, Remco J. Renken, Ben M. Harvey, Gustavo Deco, Frans W. Cornelissen, and Matthieu Gilson. 2020. "Propagation of BOLD Activity Reveals Task-Dependent Directed Interactions Across Human Visual Cortex." *Cerebral Cortex* 30 (11): 5899–5914.

Haak, Koen V., Frans W. Cornelissen, and Antony B. Morland. 2012. "Population Receptive Field Dynamics in Human Visual Cortex." *PloS One* 7 (5): e37686.

Haak, Koen V., Jonathan Winawer, Ben M. Harvey, Remco Renken, Serge O. Dumoulin, Brian A. Wandell, and Frans W. Cornelissen. 2013a. "Connective Field Modeling." *NeuroImage*. https://doi.org/10.1016/j.neuroimage.2012.10.037.

———. 2013b. "Connective Field Modeling." *NeuroImage* 66 (February): 376–84.

Haak, K. V., A. B. Morland, and F. W. Cornelissen. 2013. "Connective Field Estimates in the Cortical Lesion Project Zone of Individuals with Macular Degeneration." *Journal of Vision*. https://doi.org/10.1167/13.15.11.

Halbertsma, Hinke N., Koen V. Haak, and Frans W. Cornelissen. 2019. "Stimulus- and Neural-Referred Visual Receptive Field Properties Following Hemispherectomy: A Case Study Revisited." *Neural Plasticity* 2019 (September): 6067871.

Invernizzi, Azzurra, Koen V. Haak, Joana C. Carvalho, Remco J. Renken, and Frans W. Cornelissen. 2020. "Bayesian Connective Field Modeling: A Markov Chain Monte Carlo Approach." https://doi.org/10.1101/2020.09.03.281162.

Knapen, Tomas. 2020. "Visual Topographic Organization in Human Hippocampus Revealed by Connective Field Modelling during Naturalistic Vision and Resting State." *Journal of Vision* 20 (11): 984–984.

Kolk, Anja G. van der, Anja G. van der Kolk, Jeroen Hendrikse, Jaco J. M. Zwanenburg, Fredy Visser, and Peter R. Luijten. 2013. "Clinical Applications of 7T MRI in the Brain." *European Journal of Radiology*. https://doi.org/10.1016/j.ejrad.2011.07.007.

Liu, Jia, Daniel J. Nordman, and William Q. Meeker. 2016. "The Number of MCMC Draws Needed to Compute Bayesian Credible Bounds." *The American Statistician*. https://doi.org/10.1080/00031305.2016.1158738.

Logothetis, Nikos K., and Brian A. Wandell. 2004. "Interpreting the BOLD Signal." *Annual Review of Physiology*. https://doi.org/10.1146/annurev.physiol.66.082602.092845.

Logothetis, N. K., J. Pauls, M. Augath, T. Trinath, and A. Oeltermann. 2001. "Neurophysiological Investigation of the Basis of the fMRI Signal." *Nature* 412 (6843): 150–57.

Matsui, Teppei, Tomonari Murakami, and Kenichi Ohki. 2016. "Transient Neuronal Coactivations Embedded in Globally Propagating Waves Underlie Resting-State Functional Connectivity." *Proceedings of the National Academy of Sciences of the United States of America* 113 (23): 6556–61.

McGraw, Kenneth O., and S. P. Wong. 1996. "Forming Inferences about Some Intraclass Correlation Coefficients." *Psychological Methods*. https://doi.org/10.1037/1082-989x.1.1.30.

Nestares, O., and D. J. Heeger. 2000. "Robust Multiresolution Alignment of MRI Brain Volumes." *Magnetic Resonance in Medicine: Official Journal of the Society of Magnetic Resonance in Medicine / Society of Magnetic Resonance in Medicine* 43 (5): 705–15.

O'Herron, Philip, Pratik Y. Chhatbar, Manuel Levy, Zhiming Shen, Adrien E. Schramm, Zhongyang Lu, and Prakash Kara. 2016. "Neural Correlates of Single-Vessel Haemodynamic Responses in Vivo." *Nature*. https://doi.org/10.1038/nature17965.

Pang, J. C., P. A. Robinson, K. M. Aquino, and N. Vasan. 2017. "Effects of Astrocytic Dynamics on Spatiotemporal Hemodynamics: Modeling and Enhanced Data Analysis." *NeuroImage* 147 (February): 994–1005.

Pelli, D. G. 1997. "The VideoToolbox Software for Visual Psychophysics: Transforming Numbers into Movies." *Spatial Vision* 10 (4): 437–42.

Perinetti, Giuseppe. 2018. "StaTips Part IV: Selection, Interpretation and Reporting of the Intraclass Correlation Coefficient." *South European Journal of Orthodontics and Dentofacial Research*. https://doi.org/10.5937/sejodr5-17434.

Pisauro, M. Andrea, Neel T. Dhruv, Matteo Carandini, and Andrea Benucci. 2013. "Fast Hemodynamic Responses in the Visual Cortex of the Awake Mouse." *The Journal of Neuroscience: The Official Journal of the Society for Neuroscience* 33 (46): 18343–51.

Polimeni, Jonathan R., and Kâmil Uludağ. 2018. "Neuroimaging with Ultra-High Field MRI: Present and Future." *NeuroImage* 168 (March): 1–6.

Pruim, Raimon H. R., Maarten Mennes, Jan K. Buitelaar, and Christian F. Beckmann. 2015. "Evaluation of ICA-AROMA and Alternative Strategies for Motion Artifact Removal in Resting State fMRI." *NeuroImage* 112 (May): 278–87.

Räth, C., and R. Monetti. 2009. "Surrogates with Random Fourier Phases." *Topics on Chaotic Systems*. https://doi.org/10.1142/9789814271349_0031.

Schreiber, Thomas, and Andreas Schmitz. 1996. "Improved Surrogate Data for Nonlinearity Tests." *Physical Review Letters*. https://doi.org/10.1103/physrevlett.77.635.

Shi, Zhaoyue, Ruiqi Wu, Pai-Feng Yang, Feng Wang, Tung-Lin Wu, Arabinda Mishra, Li Min Chen, and John C. Gore. 2017. "High Spatial Correspondence at a Columnar Level between Activation and Resting State fMRI Signals and Local Field Potentials." *Proceedings of the National Academy of Sciences of the United States of America* 114 (20): 5253–58.

Shoukri, Mohamed M., Dilek Colak, Namik Kaya, and Allan Donner. 2008. "Comparison of Two Dependent within Subject Coefficients of Variation to Evaluate the Reproducibility of Measurement Devices." *BMC Medical Research Methodology* 8 (April): 24.

"Surrogate Data for Hypothesis Testing of Physical Systems." 2018. *Physics Reports* 748 (July): 1–60.

Thielen, Jordy, Umut Güçlü, Yagmur Güçlütürk, Luca Ambrogioni, Sander E. Bosch, and Marcel A. J. van Gerven. 2019. "DeepRF: Ultrafast Population Receptive Field Mapping with Deep Learning." *Cold Spring Harbor Laboratory*. https://doi.org/10.1101/732990.

Winawer, J., H. Horiguchi, R. A. Sayres, K. Amano, and B. A. Wandell. 2010. "Mapping hV4 and Ventral Occipital Cortex: The Venous Eclipse." *Journal of Vision*. https://doi.org/10.1167/10.5.1.

Zeidman, Peter, Edward Harry Silson, Dietrich Samuel Schwarzkopf, Chris Ian Baker, and Will Penny. 2018. "Bayesian Population Receptive Field Modelling." *NeuroImage* 180 (Pt A): 173–87.

SUPPLEMENTARY FIGURES

To check the possible influence of the ICA-AROMA denoise procedure, the same quantification analysis was computed on non-denoised RS data. Similar maps (Figure 1S) and correlation values (Table 1S) were observed indicating that the ICA-AROMA denoise procedure on RS-fMRI data did not influence the final CF outcomes.

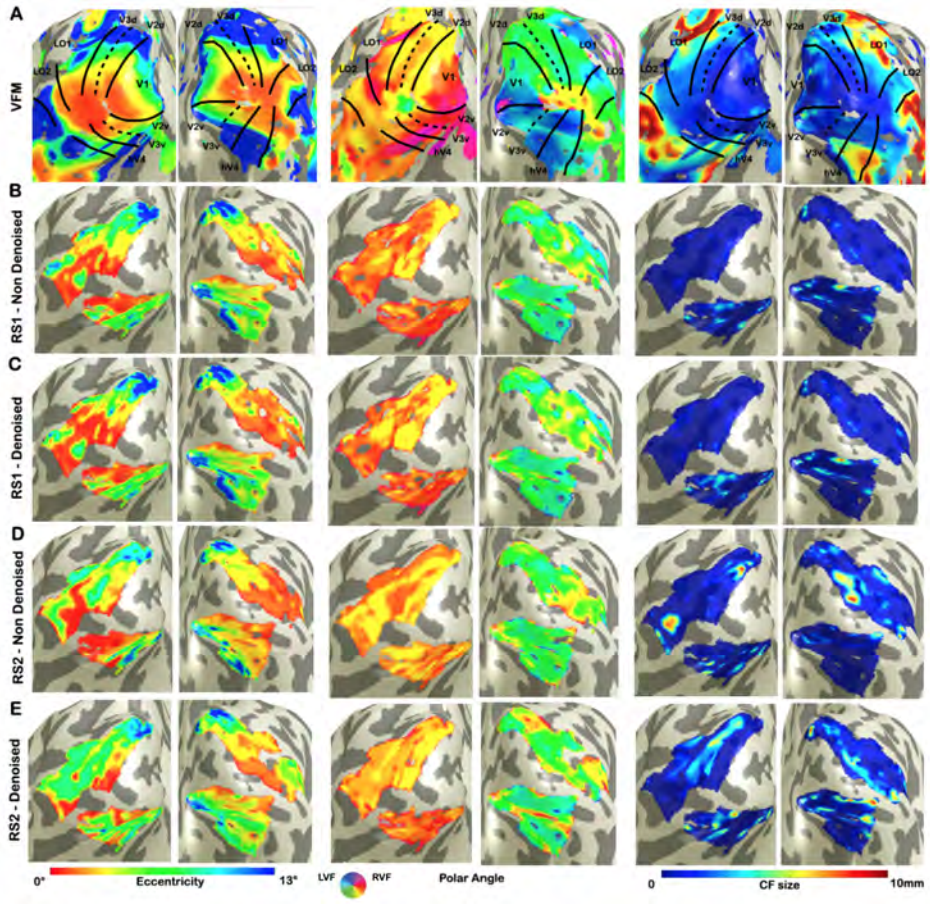

Figure 1S. Visualization of CF maps of non-denoised and denoised RS data for a single subject. From left to right: eccentricity, polar angle and CF size. Panel A corresponds to VFM derived estimates. It is reported to serve as reference for estimates obtained using RS data. Panels B and D show CF parameters for each RS run before applying ICA-AROMA denoising procedure. While panels C and E show CF estimates for RS1 and RS2 after applying the denoised procedure.

Eccentricity				
ROIs	RS1		RS2	
	Non Denoised versus Denoised		Non Denoised versus Denoised	
	R	p-value	R	p-value
V1 --> V2	0.292	p<0.001	0.0763	0.0247
V1 --> V3	0.1353	0.0003	0.1059	0.0366
V1 -> hV4	0.2124	0.0251	0.1923	0.1068
V1 -> LO1	0.1808	0.0472	-0.037	0.0912
V1 -> LO2	0.0787	0.3095	0.0077	0.5983
Polar Angle				
ROIs	RS1		RS2	
	Non Denoised versus Denoised		Non Denoised versus Denoised	
	R	p-value	R	p-value
V1 --> V2	0.362	p<0.001	0.2609	p<0.001
V1 --> V3	0.2451	p<0.001	0.3094	p<0.001
V1 -> hV4	0.3487	p<0.001	0.0862	0.1191
V1 -> LO1	0.3017	p<0.001	-0.041	0.6232
V1 -> LO2	0.2959	0.008	0.0048	0.5649

Table 1S. Correlation between non-denoised and denoised CF maps obtained from RS data at group level. To estimate and compare the level of agreement between not-denoised and denoised CF maps that were obtained from RS1 and RS2 scans by using the standard CF model, we computed the Pearson's correlations for the eccentricity (*rho*) and the circular correlation for the polar angle (*theta*) parameters. In order to compute the correlation scores, eccentricity and polar angle parameters were estimated at single subject level and then concatenated across all participants.

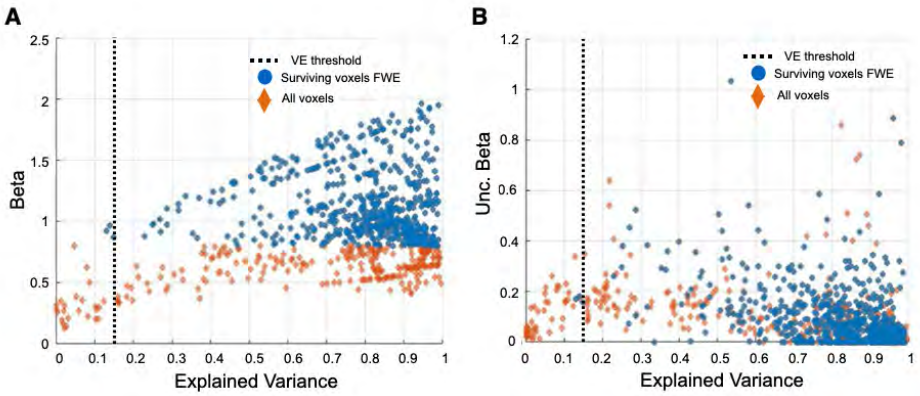

Figure 2S. Comparison of thresholding approaches on a single subject level in V1>V2 area using RS1 data.
In Panel **A**, the relation between VE and the beta parameter is presented for all the voxels (orange diamonds) and only for the ones surviving the 95% CI FWE beta-threshold (blue dots). The standard VE threshold is not applied but indicated by a black dotted line. In Panel **B**, the relation between VE and the uncertainty associated with beta is presented.

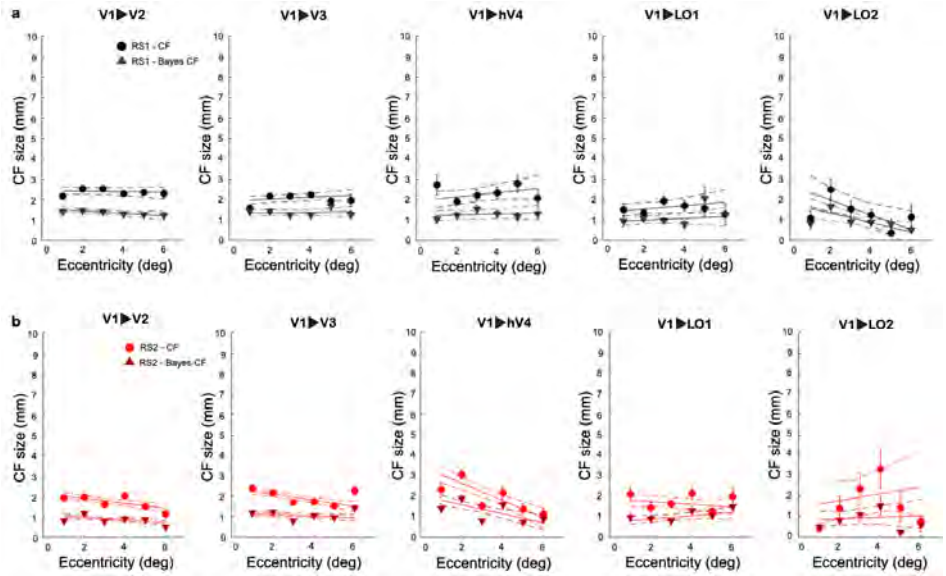

Figure 3S. Connective field size as a function of pRF eccentricity for RS scans. For standard and Bayesian CF models, eccentricity was binned in intervals of 1 deg and a linear fit was applied. The CF size was initially weighted with variance explained higher than 0.15. Each dot and triangle indicate the mean of the CF size for each bin. While the dashed lines correspond to the 95% bootstrap confidence interval of the linear fit. In Panel **A**, CF models were applied to RS1 scan while, in panel **B** to RS2 scan.

Table 2S. Within-subject variability of CF parameter estimates.

Eccentricity					Polar Angle				
V1 > V2	RS1		RS2		V1 > V2	RS1		RS2	
	Standard CF	MCMC CF	Standard CF	MCMC CF		Standard CF	MCMC CF	Standard CF	MCMC CF
sub1	0.6041	0.6168	0.5982	0.6087	sub1	0.5967	0.5847	0.4975	0.4835
sub2	0.4289	0.3591	0.3788	0.3831	sub2	0.7881	0.7816	0.6632	0.585
sub3	0.6059	0.5982	0.6099	0.5879	sub3	0.5281	0.5111	0.4904	0.4921
sub4	0.4592	0.434	0.5008	0.4773	sub4	0.6768	0.586	0.6838	0.6933
sub5	0.5061	0.498	0.5415	0.5343	sub5	0.6582	0.6604	0.6482	0.6533
sub6	0.5247	0.5255	0.6121	0.6055	sub6	0.366	0.3461	0.4629	0.4349
sub7	0.5014	0.4718	0.5099	0.5425	sub7	0.2371	0.2598	0.6426	0.6845
sub8	0.7656	0.7639	0.6928	0.67	sub8	0.7514	0.7573	0.6609	0.6571
sub9	0.516	0.5207	0.4651	0.4561	sub9	0.7687	0.8129	0.6615	0.6946
sub10	0.8177	0.7275	0.7449	0.7424	sub10	0.5176	0.4875	0.4887	0.5002
sub11	0.4719	0.455	0.4962	0.4879	sub11	0.4174	0.4228	0.4123	0.466
sub12	0.6945	0.6986	0.6202	0.6218	sub12	0.8659	0.8434	0.7764	0.7758
V1 > V3	Standard CF	MCMC CF	Standard CF	MCMC CF	V1 > V3	Standard CF	MCMC CF	Standard CF	MCMC CF
sub1	0.4603	0.4711	0.5611	0.5309	sub1	0.7438	0.751	0.5269	0.5182
sub2	0.5583	0.4778	0.3524	0.354	sub2	0.9487	1.0093	0.5867	0.571
sub3	0.4518	0.4575	0.4717	0.4765	sub3	0.747	0.7454	0.6618	0.6952
sub4	0.4397	0.4053	0.4773	0.4702	sub4	0.7172	0.6134	0.8307	0.8071
sub5	0.4741	0.4749	0.4874	0.4885	sub5	0.7118	0.7204	0.6634	0.6146
sub6	0.6169	0.6376	0.6873	0.6626	sub6	0.2893	0.2643	0.6059	0.6099
sub7	0.4977	0.4137	0.6137	0.6241	sub7	0.2491	0.282	0.674	0.7467
sub8	0.702	0.6898	0.5725	0.5604	sub8	0.6118	0.6089	0.4903	0.5178
sub9	0.4956	0.4956	0.4392	0.412	sub9	0.7956	0.8247	0.7893	0.8048
sub10	0.7669	0.7155	0.7238	0.7511	sub10	1.0817	0.9427	0.7521	0.8018
sub11	0.3979	0.416	0.4218	0.4212	sub11	0.8994	0.8481	0.7369	0.7225
sub12	0.5977	0.5834	0.5667	0.5789	sub12	0.884	0.881	0.5676	0.5641
V1 > hV4	Standard CF	MCMC CF	Standard CF	MCMC CF	V1 > hV4	Standard CF	MCMC CF	Standard CF	MCMC CF
sub1	0.6803	0.5514	0.6843	0.6709	sub1	0.7339	0.5723	0.4696	0.4547
sub2	0.7155	0.3835	0.4345	0.4638	sub2	0.3995	0.4733	0.6886	0.6467
sub3	0.5993	0.5699	0.4046	0.4228	sub3	0.3161	0.3195	0.4269	0.5167
sub4	0.4081	0.3993	0.4535	0.4314	sub4	0.5725	0.5617	0.6375	0.6698
sub5	0.6453	0.6517	0.361	0.3569	sub5	0.5036	0.5169	0.3745	0.2899
sub6	0.5209	0.4817	0.9185	0.9595	sub6	0.1608	0.1561	0.7456	0.7732
sub7	0.5219	0.4745	0.7038	0.7461	sub7	0.1106	0.0835	0.2249	0.228
sub8	0.5915	0.5477	0.6996	0.6797	sub8	0.4678	0.4568	0.429	0.512
sub9	0.488	0.4699	0.5545	0.3309	sub9	0.7568	0.7553	0.8493	0.9329
sub10	0.8293	0.338	0.3744	0.4632	sub10	0.8133	0.3699	0.3988	0.4486
sub11	0.5025	0.3745	0.4939	0.4956	sub11	0.4064	0.1668	0.3861	0.3564
sub12	0.8573	0.7866	0.9118	0.8963	sub12	1.1269	1.0395	0.4766	0.466
V1 > LO1	Standard CF	MCMC CF	Standard CF	MCMC CF	V1 > LO1	Standard CF	MCMC CF	Standard CF	MCMC CF
sub1	0.2957	0.3212	0.4511	0.3655	sub1	0.7714	1.0436	1.0286	0.997
sub2	0.6151	0.6417	0.1581	0.167	sub2	1.1331	0.6344	0.2463	0.2573
sub3	0.4004	0.3685	0.3895	0.3744	sub3	1.1454	1.337	0.9311	0.7291
sub4	0.4696	0.4613	0.5243	0.5156	sub4	0.997	0.9376	1.4503	1.464
sub5	0.5664	0.5902	0.3486	0.3216	sub5	0.8792	0.8429	0.5201	0.4817
sub6	0.5093	0.3655	0.9833	0.9179	sub6	0.1371	0.0719	1.2361	1.2842
sub7	0.5554	0.5631	0.6132	0.5848	sub7	0.4587	0.4373	0.7042	0.7373
sub8	1.473	1.5283	0.7314	0.5999	sub8	0.6043	0.572	0.569	0.4727
sub9	0.6907	0.6924	0.6877	0.9959	sub9	0.616	0.6355	0.1301	0.166
sub10	0.7547	0.3716	0.8081	0.8268	sub10	0.4037	0.4244	0.5949	0.5881
sub11	0.6004	0.5245	0.4417	0.421	sub11	0.7894	0.7604	1.0417	1.0394
sub12	0.3531	0.3709	0.8008	0.8169	sub12	0.5541	0.7711	0.3569	0.391
V1 > LO2	Standard CF	MCMC CF	Standard CF	MCMC CF	V1 > LO2	Standard CF	MCMC CF	Standard CF	MCMC CF
sub1	0.0979	0.1385	0.5747	0.6199	sub1	0.1007	0.1215	0.8105	0.7892
sub2	0.5392	0.5365	0.2286	0.2218	sub2	0.4958	0.3849	0.4824	0.4519
sub3	0.5016	0.5164	0.304	0.2323	sub3	1.0287	1.0428	0.5166	0.3704
sub4	0.4251	0.4276	0.4635	0.4391	sub4	0.5652	0.5514	1.1707	1.2203
sub5	0.453	0.4733	0.275	0.2578	sub5	0.6998	0.7054	0.2904	0.4427
sub6	0.4474	0.2758	0.431	0.3575	sub6	0.0767	0.0513	0.2398	0.3694
sub7	0.6104	0.6019	0.6052	0.6216	sub7	0.6528	0.7378	0.6285	0.6526
sub8	0.3177	0.2784	0.5604	0.4616	sub8	0.0839	0.0779	0.4074	0.3213
sub9	0.5182	0.4935	0.2362	0.2362	sub9	0.5656	0.6322	0.1387	0.1387
sub10	0.1187	0.1199	0.3165	0.3103	sub10	0.0091	0.009	0.7048	0.8607
sub11	0.9313	0.6467	0.2447	0.4321	sub11	0.4989	0.5146	0.2218	0.3629
sub12	0.059	0.2433	0.001	0.0021	sub12	0.1179	1.0552	0.002	0.0021

For standard and Bayesian CF models, we estimated the coefficient of variation to evaluate the within-subject reproducibility of eccentricity and polar angle estimates for both RS scans. The coefficient of variation is reported for each visual area and for each participant.

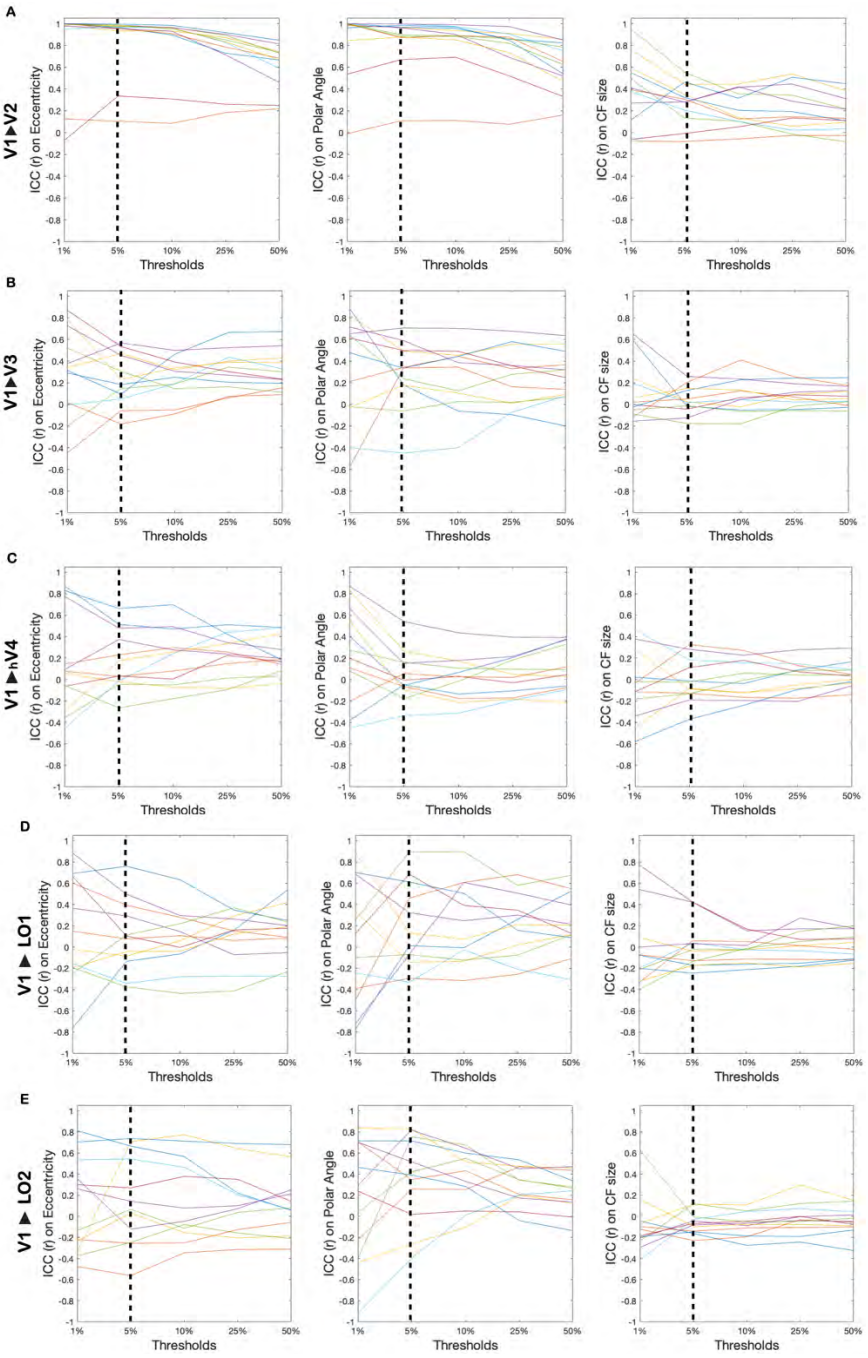

Figure 4S. Evaluation of different VE thresholds on ICC. In order to evaluate a viable VE threshold applied on the test-retest analysis, we evaluate the influence of using five different % of strongest activated voxels based on VE (1%, 5%, 10%, 25% and 50%) on the final ICC (r) across ROIs (Panels A, B, C, D and E). Each participant is represented by a colored lines.

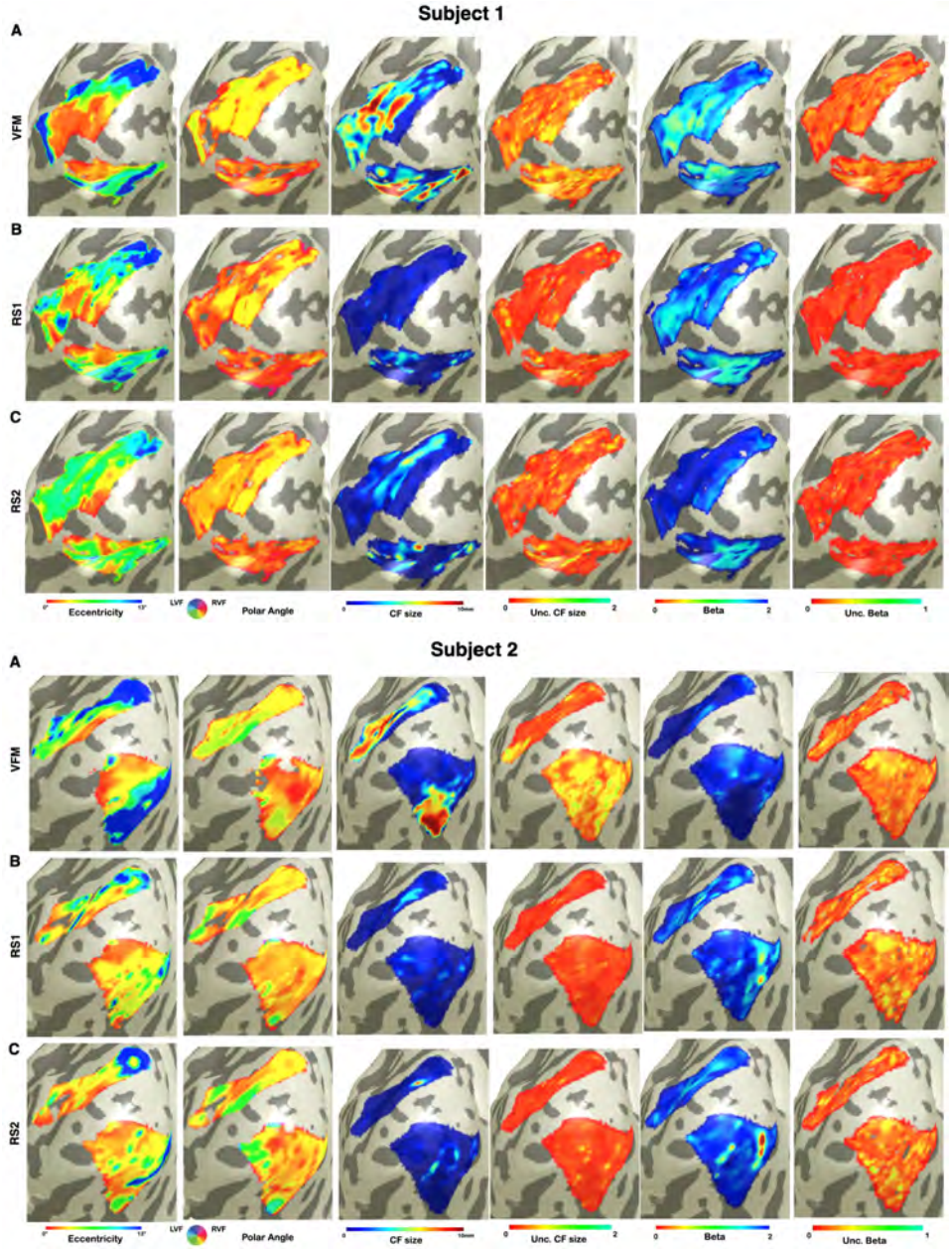

Figure 5S. Visualization of CF and uncertainty maps of VFM and RS data for two participants. From left to right: eccentricity, polar angle, CF size, uncertainty of CF size, Beta and Uncertainty of Beta. Panel A corresponds to VFM derived estimates. While panels B and C show CF estimates for RS1 and RS2.